Two-dimensional prognostic experiments for fast-flowing ice streams from the Academy of Sciences Ice Cap

Y.V. Konovalov, O.V. Nagornov

Mathematical Department, National Research Nuclear University MEPhI (Moscow Engineering Physics Institute), Kashirskoe shosse, 31, 115409, Moscow, Russian Federation

Correspondence to: Y.V. Konovalov (yu-v-k@yandex.ru)

Abstract

The prognostic experiments for fast-flowing ice streams on the southern side of the Academy of Sciences Ice Cap in the Komsomolets Island, Severnaya Zemlya archipelago, are implemented in this study. These experiments are based on inversions of basal friction coefficients using a two-dimensional flow-line thermo-coupled model and the Tikhonov's regularization method. The modeled ice temperature distributions in the cross-sections were obtained using the ice surface temperature histories that were inverted previously from the borehole temperature profile derived at the summit of the Academy of Sciences Ice Cap and employing elevational gradient of ice surface temperature changes, which is equal to about 6.5 ^{0}C km^{-1}. Input data included InSAR ice surface velocities, ice surface elevations, and ice thicknesses obtained from airborne measurements and the surface mass balance, were adopted from previous investigations for the implementation of both the forward and inverse problems. The prognostic experiments reveal that both ice mass and ice stream extents decline for the reference time-independent surface mass

balance. Specifically, the grounding line retreats (a) along the B–B′ flow line from ~40 km to ~30 km (the distance from the summit), (b) along the C–C′ flow line from ~43 km to ~37 km, and (c) along the D–D′ flow line from ~41 km to ~32 km considering a time period of 500 years and assuming time-independent surface mass balance. Ice flow velocities in the ice streams decrease with time and this trend results in the overall decline of the outgoing ice flux. Generally, the modeled evolution is in agreement with observations of deglaciation of Severnaya Zemlya archipelago.

1. Introduction

There are relevant diagnostic observations of glaciers such as digital Landsat imagery and satellite synthetic aperture radar interferometry (InSAR), airborne measurements, borehole ice temperature and ice surface mass balance measurements. These observations provide data for prognostic experiments that allow prediction of future glacier conditions for different climatic scenarios in the future. These experiments can be performed employing the mathematical modeling and in this study a two-dimensional ice flow model is applied for prediction of the future conditions of fast-flowing ice streams on the southern side of the Academy of Sciences Ice Cap in the Komsomolets Island, Severnaya Zemlya archipelago (Figure 1; Dowdeswell et al., 2002).

The observations were based on digital Landsat imagery and satellite synthetic aperture radar interferometry (InSAR) and revealed four drainage basins and four fast-flowing ice streams on the southern side of the Academy of Sciences Ice Cap in the Komsomolets Island, Severnaya Zemlya archipelago (Figure 2; Dowdeswell et al., 2002). The four ice streams are 17−37 km long and 4–8 km wide (Dowdeswell et al., 2002). Bedrock elevations of these areas are below the sea level, and the ice flow velocities attain a value of 70–140 m/a (Figure 2). Such fast flow-line features are typical for outlet glaciers and ice streams in both the Arctic and the Antarctic. These ice streams are the major locations of iceberg calving from the Academy of Sciences Ice Cap (Dowdeswell et al., 2002).

The flow-line profiles of the three ice streams on the southern side of the Academy of Sciences Ice Cap are shown in Figure 3. Ice flow in these ice streams is simulated with a two-dimensional flow-line higher-order finite-difference model (e.g., Colinge and Blatter, 1998; Pattyn, 2000, 2002). This model describes an ice flow along a flow line (Pattyn, 2000, 2002). The results of the diagnostic experiments obtained in (Konovalov, 2012), for instance, for the C–C′ flow-line profile show that the ice surface velocity along the flow line attains a value of 100 m/a assuming that ice is sliding. However, the observed surface velocity distribution along the C–C′ flow-line profile (Dowdeswell et al., 2002) is not similar to that obtained by the model experiments for constant values of friction coefficient and for both linear and nonlinear friction laws (Konovalov, 2012). Similarly, the diagnostic experiments carried out for the B–B′ and D–D′ profile data show the same results for the ice flow velocities. The deviation between the observed and modeled surface velocities suggests that the friction coefficient should be a spatially variable parameter. Therefore, to achieve a better agreement between the observed and simulated velocities, the spatial distribution of the friction coefficients requires to be optimized and an inverse problem needs to be solved (e.g., MacAyeal, 1992; Sergienko et al., 2008; Arthern and Gudmundsson, 2010; Gagliardini et al., 2010; Habermann et al., 2010; Morlighem et al., 2010; Jay-Allemand et al., 2011; Larour et al., 2012; Sergienko and Hindmarsh, 2013).

The inversion of friction coefficients is based on the minimization of the deviation between the observed and modeled surface velocities. A series of test experiments (Konovalov, 2012), in which modeled surface velocities are used as observations in the inverse problem, have shown that the inverse problem for the full 2D ice flow-line model is ill posed. More precisely, the surface velocity is weakly sensitive to small perturbations in friction coefficients, and as a result the perturbations appear in the inverted friction coefficients (Konovalov, 2012).

Herein, in the prognostic experiments we use the friction coefficients inversions obtained by applying the Tikhonov's regularization method, in which Tikhonov's stabilizing functional is added to the main discrepancy functional (Tikhonov and Arsenin, 1977).

The inversions of friction coefficient are used in the prognostic experiments for the fast-flowing ice streams. The considered 2D prognostic experiments are the numerical simulations with the ice thickness distribution changes performed by the 2D flow-line thermo-coupled model, which includes diagnostic equations as the heat-transfer equation and the mass-balance equation (Pattyn, 2000, 2002). In this study, we present the results of the prognostic experiments performed for the B–B′, C–C′, and D–D′ profiles (Figure 3). Specifically, the prognostic experiments are carried out for the three ice streams (Figure 2) that are the main sources of the ice flux from the ice cap to the ocean. The results of the prognostic experiments include future modeled histories of ice thickness distributions along the flow lines of grounding line locations and outgoing ice fluxes. The surface mass balance in the performed experiments is considered as time-independent, so the prognostic experiments show the assessment of the minimal ice mass loss in the ice streams in the future, because the obtained forecasts don't include for future global warming. Nevertheless, the results of the prognostic experiments are in agreement with the observations of ice mass loss on the Severnaya Zemlya archipelago (Moholdt et al., 2012).

2. Field equations

2.1. Forward problem: Diagnostic equations

The 2D flow-line higher-order model includes the continuity equation for incompressible medium, the mechanical equilibrium equation in terms of stress deviator components (Pattyn, 2000, 2002), and the rheological Glen law (Cuffey and Paterson, 2010):

$$\begin{cases} \int\limits_{h_b}^{z} \frac{\partial u}{\partial x} dz' + \frac{1}{b}\frac{d\,b}{d\,x}\int\limits_{h_b}^{z} u\,dz' + w - w_b = 0, \\ 2\frac{\partial \sigma'_{xx}}{\partial x} + \frac{\partial \sigma'_{yy}}{\partial x} + \frac{\partial^2}{\partial x^2}\int\limits_{z}^{h_s} \sigma'_{xz}\,dz + \frac{\partial \sigma'_{xz}}{\partial z} = \rho g \frac{\partial h_s}{\partial x}, \\ \sigma'_{ik} = 2\eta\dot{\varepsilon}_{ik}; \quad \eta = \frac{1}{2}\left(m\,A(T)\right)^{-\frac{1}{n}} \dot{\varepsilon}^{\frac{1-n}{n}}, \\ 0 < x < L;\; h_b(x) < z < h_s(x), \end{cases} \tag{1}$$

where (x,z) is a rectangular coordinate system with the x-axis along the flow line and the z-axis pointing vertically upward; u, w are the horizontal and vertical ice flow velocities, respectively; b is the width along the flow-line, σ'_{ik} is the stress deviator; $\dot{\varepsilon}_{ik}$ is the strain-rate tensor; $\dot{\varepsilon}$ is the second invariant of the strain-rate tensor; ρ is the ice density; g is the gravitational acceleration; η is the ice effective viscosity; $A(T)$ is the flow-law rate factor; T is the ice temperature; $h_b(x)$, $h_s(x)$ are the ice bed and ice surface elevations, respectively; and L is the glacier length.

The boundary conditions and some complementary experiments that were carried out applying this model, were considered in (Konovalov, 2012). In particular, the technique, when the boundary conditions have been included in the momentum equations (Konovalov, 2012), was applied in the considered here prognostic experiments.

2.2. Inverse problem for the friction coefficient

The inversion of friction coefficient has been carried out using the gradient minimization procedure for the "smoothing" functional (Tikhonov and Arsenin, 1977):

$$F = \int_0^L (u_{\mathrm{obs}} - u_{\mathrm{mod}})^2 \, dx + \beta \int_0^L \left(K_{\mathrm{fr}}^2 + q(x) \left(\frac{d K_{\mathrm{fr}}}{d x} \right)^2 \right) dx, \qquad (2)$$

where u_{obs} are the observed velocities along the flow line and u_{mod} are the modeled velocities, the first integral Φ is the discrepancy and the second integral Ω is the stabilizer (Tikhonov and Arsenin, 1977), β is the regularization parameter, and $q(x)$ is considered equal to 1. The nonzero value of β implies that the inverse problem, i.e., the problem that is based on the minimization of the discrepancy Φ, is ill posed and the original problem of the discrepancy minimization is replaced with the problem of the smoothing functional minimization.

The details of the gradient minimization procedure and the problem of the regularization parameter choice are discussed in (Nagornov et al., 2006; Konovalov, 2012). In this manuscript the inversions have been obtained for the linear (viscous) friction law, implying the experiments implemented in (Konovalov, 2012) with the inversions for the C-C' profile, that have shown a good agreement between the observed (u_{obs}) and the calculated (u_{mod}) surface velocities for the linear friction law.

2.3. Prognostic equations

The thermo-coupled prognostic experiments imply that the 2D flow-line model includes the heat-transfer equation (Pattyn, 2000, 2002):

$$\frac{\partial T}{\partial t}=\chi\left(\frac{\partial^2 T}{\partial x^2}+\frac{1}{b}\frac{db}{dx}\frac{\partial T}{\partial x}+\frac{\partial^2 T}{\partial z^2}\right)-\left(u\frac{\partial T}{\partial x}+w\frac{\partial T}{\partial z}\right)+\frac{2A^{-\frac{1}{n}}\dot{\varepsilon}^{\frac{1+n}{n}}}{\rho C}, \qquad (3)$$

where χ and C are the thermal diffusivity and the specific heat capacity, respectively. The terms in the first and in the second brackets respectively define the heat transfer due to heat diffusion and due to ice advection. The last term is associated with strain heating.

In this model it is suggested that the ice surface temperature at the Academy of Sciences Ice Cap varies with an elevational gradient of temperature changes, which is equal to about $6.5\ {}^0\mathrm{C/km}$. Hence, the ice surface temperature distribution along the flow line is defined by the temperature history at the summit $T_{s0}(t)$ and by the elevational changes, and it is expressed as

$$T_s(x,t)=T_{s0}(t)+\theta_T\,(h_s(0)-h_s(x)), \qquad (4)$$

where θ_T is the elevational gradient. Therefore, Equation (4) provides the boundary condition on the ice surface. However, it should be noted that Eq. (4) does not account firn warming through refreezing meltwater.

The boundary condition at the ice base is defined by the geothermal heat flux and by the heating due to the basal friction, and it is expressed as (Pattyn, 2000, 2002)

$$\frac{\partial T}{\partial z}=-\frac{1}{k}\left(Q+(\sigma'_{xz})_b u_b\right), \qquad (5)$$

where k is the thermal conductivity.

The boundary conditions at the ice (ice-shelf) terminus and at the ice-shelf base are defined by sea water temperature, which is considered as $-2\,^\circ\mathrm{C}$ in this study.

The ice thickness temporal changes along the flow line are described by the mass-balance equation (Pattyn, 2000, 2002):

$$\frac{\partial H}{\partial t} = M_s - M_b - \frac{1}{b}\frac{\partial (\bar{u}\, b\, H)}{\partial\, x}, \qquad (6)$$

where $\bar{u}$ is the depth-averaged horizontal velocity, M_s is the annual surface mass balance, and M_b is the melting rate at the ice base.

The mass-balance equation requires two boundary conditions at the summit and at the ice terminus. The first condition at the ice cap summit implies that $\frac{\partial h_s}{\partial x} = 0$. The second condition applied in the ice terminus originates from the fact that the ice thicknesses in the ice shelf along the flow line attain a constant value at the terminus.

2.3. Grounding line evolution

In the model the grounding line position is defined from the hydrostatic equilibrium (Schoof, 2007; Pattyn et al., 2012; Seroussi et al., 2014). That is, since sea water flow under ice shelf is not considered in the model and, hence, the pressure in Eq. (10)-(11) from Pattyn et al. (2012) is equal to hydrostatic pressure, the grounding line position is at the location where

$$-\rho_w\, h_r = H\, \rho \qquad (7)$$

and h_r is the bedrock elevation, ρ_w is the water dencity.

3. Results of the numerical experiments

3.1 Inversions for the friction coefficient

For the first run of the friction coefficient inversions, the linear ice temperature profile approximation is applied. Specifically, it is assumed that the ice temperature linearly increases from −15°C at the surface to −5°C at the ice base at the division and increases from −2°C to −1°C at the grounding line. Figure 4(a) shows the inverted friction coefficient distribution along the C–C′ flow line. The retrieved friction coefficient gradually decreases from ~3.5 × 10^3 Pa a m^{-1} to a mean value of 5 × 10^2 Pa a m^{-1} within a distance of around 25 km < x <40 km (Figure 4(a)). The difference between the simulated and *observed* surface velocities is relatively small (Figure 4(b)) (Konovalov, 2012).

The inverted friction coefficient distributions along the B–B′ and D–D′ flow lines show qualitatively the same trends, i.e., they gradually decrease along the flow line from a high to a lower level.

After the first run of the inversions, the ice temperature simulations are performed for inverted friction coefficients and boundary conditions (4) and (5). Boundary condition (4) includes the temperature history $T_{s0}(t)$. In particular, if the history is the past temperature (Nagornov et al., 2005, 2006), which was inverted previously from the borehole temperature profile derived at the summit of the Academy of Sciences Ice Cap (Zagorodnov, 1988; Arkhipov, 1999), i.e. the temperature history over the past 1000 years to present day (Nagornov et al., 2005, 2006), - then we would expect the simulated output temperature close to the real present temperature in the ice stream along the flow line. In other words, the modeled temperature will be close to the present temperature (in the year when borehole measurements were performed), assuming a good agreement between the model results and the real physical processes that occur in the glacier, which are in general described by the model. The past surface temperature history, which was applied in the simulations of the present ice temperature, was adopted from Nagornov et al. (2005, 2006). The modeled present temperature distributions along the B–B′, C–C′ and D–D′ cross-sections are shown in Figure 5.

For the second run of the basal friction coefficient inversions, the modeled temperature distributions are applied (the modeled temperature is defined from Eq. (3)..(5)). The inverted friction coefficients (i) for the linearly approximated ice temperature and (ii) for the modeled ice temperature are shown in Figure 6. Generally, the distinctions in the friction coefficients are insignificant, and, therefore, the ice temperature approximations can be applied in the inverse problem as the first iteration of the ice temperature distribution in the glacier.

3.2. Prognostic experiments

The main input data along with flow-line profiles for the prognostic experiments, namely, the surface mass balance, are adopted from Bassford et al. (2006). Figure 7 shows the elevational mass-balance distribution along the C–C′ flow line, i.e., it shows how the surface mass balance changes with elevation in the C–C′ direction (Bassford et al., 2006). For the B–B′ and D–D′ flow lines, the elevational mass-balance distributions are qualitatively the same (Bassford et al., 2006). In the prognostic experiments that have been carried out, the mass balance is considered as time-independent. That is, the elevational mass-balance distributions are kept unchanged for the considered time period in the future. Thus, we intend to assess the maximum ice thickness in the ice streams in the future, because the forecasts implemented with the time-independent surface mass balance, don't imply a future global warming and, so, they don't suggest a future decreasing of the surface mass balance M_s in Eq.(6). Similarly, the ice surface temperature is suggested to be time-independent but dependent on elevation, i.e., according to Eq. (4), it is changed with elevation with a constant value of $T_{s0}(t)$. From the borehole temperature measurements, the present ice surface temperature at the summit is about $-7.2\,°\mathrm{C}$. The initial ice temperatures applied in the prognostic experiments are shown in Figure 5.

Despite that future warming scenarios are not included into the prognostic experiments, the modeled ice cap response to the present environmental impact, which is reflected in the elevational mass-balance distribution (Bassford et al., 2006), reveals that the ice thicknesses gradually diminish along all the three flow lines. Figures 8(a)–10(a) show the modeled successive ice surfaces divided into 50-year time intervals for the B–B′, C–C′, and D–D′ profiles, respectively. Figures 8(b)–10(b) show the same results as Figures 8(a)–10(a), respectively, but these complementary figures show the evolutions of the three ice shelves in more detail. The prognostic experiments are performed by applying a rectangular ice-shelf geometry. The cumulative impact of sea water, surface mass balance, and ice flow changes in the glacier has produced the future modeled ice shelve geometries. The ancillary black circles in Fig. 8(a,b)–10(a,b) are aligned with the grid nodes and, thus, they show the spatial resolution, at which the prognostic experiments have been implemented. The spatial resolution is irregular and it decreases from about $2 \cdot 10^3$ m at the summit to about 10^2 m in the grounding line vicinity and in the ice shelf. The spatial grid is considered unchangeable throughout the period of the modeling.

The grounding line history, i.e., grounding line retreat or advance, specifically reflects the growing or diminishing ice mass, i.e., the history is an indicator of the glacier evolution. The grounding line retreats (a) along the B–B′ flow line from ~40 km to ~30 km (Fig. 11 (a)), (b) along the C–C′ flow line from ~43 km to ~37 km (Fig. 11 (b)), and (c) along the D–D′ flow line from ~41 km to ~32 km (Fig. 11 (c)) considering a time period of 500 years.

Furthermore, the results of the prognostic experiments can be likewise treated suggesting a changes in the friction coefficient. The glacier terminus, currently fast flowing and therefore at pressure melting, becomes eventually frozen to the ground – ice thickness insufficient to insulate from cold athmosphere and reduced driving stress and strain heating. So basal friction coefficients could change drastically, given the simulated changes in glacier geometry.

The ice flow velocities in the ice streams decrease with time and this trend diminishes the outgoing ice fluxes in the future. Figure 12 shows the modeled outgoing ice flux histories, i.e., it shows how the value $\bar{u}\,H\,b$, which is defined at the ice-shelf terminus, changes with time. Accordingly, figure 13 shows the future history of the overall outgoing ice flux, i.e., it is the sum of the three future modeled historical trends that are shown in Fig. 12.

There are small peaks that periodically disturb main historical trends of the three outgoing ice fluxes. Every peak reflects ice calving at the ice-shelf terminus. Similarly, the ice calving provides a sudden change in the value of the outgoing ice flux ($\bar{u}\,H\,b$) due to a sudden change in the ice thickness (H) at the terminus. Considering a complex environmental impact on ice shelves (Bassis et al., 2008), from the mathematical point of view it can be suggested that the calving processes are described by a stochastic model. Hence, the overall annual (or decadal) sizes of the anticipated ice debris can be described by a frequency distribution function. In the model In the model the periodic calving of equal-size debris is considered, i.e., δ-function is considered as the frequency distribution function.

In this model the both ice-shelf length and ice-shelf thickness at the terminus are considered as the variables that should satisfy a certain conditions. If the ice-shelf length exceeds a value l_{cr} (the parameter of the model) or the ice-shelf thickness beside the terminus becomes smaller than a value H_{cr}, then the calving of the appropriate part of ice occurs in the model. To investigate the impact of the parameters on the results of the modeling, the parameters were varied in a series of the experiments. However, the simulation reveals that the mass balance, friction coefficient, ice temperature have the main impact to the assessment of the grounding line retreat derived by the modeling.

4. Discussion

Numerical experiments carried out in the 2D model using the randomly perturbed friction coefficient have revealed that the horizontal surface velocity is weakly sensitive to the perturbations (Fig. 4 from Konovalov (2012)). Thus, the perturbations appear on the *x*-distributed inverted friction coefficient. Therefore, the inverse problem should be considered as ill posed because the weak sensitivity of the surface velocity to the perturbations in the friction coefficient justifies the instability in the inverse problem. In other words, the instability in the inverse problem means that small deviations in the observed surface velocities allow significant perturbations in the friction coefficient. Hence, the application of the regularization method is justified.

The Tikhonov's method that is based on the application of the stabilizing functional reduces the effects of perturbations proportionally to the regularization parameter β (Tikhonov and Arsenin, 1977). A further increase in the parameter leads to a reduction in the real spatial variability of the friction coefficients.

The reduction in the existent friction coefficient variability is associated with a growing discrepancy between the observed and modeled surface velocities. Thus, the regularization parameter is chosen as the value at which nonexistent perturbations are reduced, but the real variability of the friction coefficient is not completely reduced by the stabilizing functional. The optimal value of the regularization parameter can be defined approximately in the curve, which is the deviation between the observed and modeled surface velocities versus the regularization parameter (Leonov, 1994; Konovalov, 2012).

Evidently, the stabilizing functional narrows down the range of possible inverted *x*-distributions of the friction coefficients. Thus, it is supposed *a priori* that the real spatial distribution of the friction coefficient with respect to the x-axis is a smooth function. Moreover, the friction coefficient in the friction laws is considered as a constant (e.g., Van der Veen, 1987; MacAyeal, 1989; Pattyn, 2000; Gudmundsson, 2011). Hence, the friction coefficient inversion performed for the three cross-sections can be interpreted as follows.

The two evidently distinguished levels in the inverted friction coefficient distributions can be explained by changing the physical properties of the bedrock along the flow lines. Similarly, the large values of the friction coefficient at 0 km < x < 20 km justify the rock-type bottom where ice is frozen to the bed (the ice temperature at 0 km < x < 20 km is lower than the melting point). The lower values of the friction coefficient at 25 km < x < 40 km presumably indicate the existence of water-saturated till layer at the bottom (e.g., Engelhardt et al., 1978; Engelhardt et al., 1979; Boulton, 1979; Boulton and Jones, 1979; MacAyeal, 1989; Engelhardt and Kamb, 1998; Iverson et al., 1998; Tulaczyk et al., 2000). Specifically, the till layer (deformable basal sediments) provides the basal ice sliding.

The modeled present ice temperatures (Figure 5) are qualitatively the same in the three cross-sections. There are resembling zones of relatively cold ice that can be distinguished in the modeled temperatures approximately in the middle (in vertical dimension) of each cross-section. These cold ice zones reflected the surface temperature minimum about 150–200 years ago in the inverted past temperature history (Nagornov et al., 2005, 2006). This surface temperature minimum corresponds to an event that is known as Little Ice Age. Thus, surface boundary conditions (4), and diffusive and advective heat transfers provide the basal ice temperature that mainly varies in the range $-4\ \text{to} -9°\text{C}$ at 25 km < x < 40 km. Therefore, the modeled basal ice temperature becomes lower than the melting point. Hence, the modeled ice temperatures justify the sliding due to the existence of till layer at the bottom (Engelhardt et al., 1978; Engelhardt et al., 1979; Boulton, 1979; Boulton and Jones, 1979; MacAyeal, 1989; Engelhardt and Kamb, 1998; Iverson et al., 1998; Tulaczyk et al., 2000).

However, note that the heat-transfer model considered here does not account for the melt water refreezing in the subsurface firn layer (Paterson and Clarke, 1978). The numerical experiments carried out in Paterson and Clarke (1978) have shown that the heat source demonstrated significant impact due to melt water refreezing of the ice temperature profiles depending on the melt water percolation depth. Thus, the notion that the basal ice temperature is higher than the modeled temprature and could reach the melting point cannot be fully excluded.

General formulations of the friction laws assume that the appropriate equations include the effective basal pressure (e.g., Budd et al., 1979; Iken, 1981; Bindschadler, 1983; Jansson, 1995; Vieli et al., 2001; Pattyn, 2000). Introduction of the hydrostatic pressure in Equation (2) does not provide a constant value of the inverted friction coefficient at $x > 25$ km. The inversion performed for the nonlinear Weertman-type friction law reveals similar variations in the inverted friction coefficient at $x > 25$ km (Konovalov, 2012). The similar variability in the inverted friction coefficients obtained for both the linear and nonlinear friction laws (Konovalov, 2012) implies that the physical properties of the bedrock layer change according to the friction coefficient distribution along the flow line. In particular, the presence of water in the bedrock layer can be explained by the low bed elevations in the areas of fast-flowing ice streams (e.g., Knight, 1999; Vieli et al., 2001) or by a hydrological processes (e.g., Röthlisberger, 1972; Nye, 1976; Hewitt, 2011; Hoffman and Price, 2014). Therefore, the water content in the bedrok layer can vary in agreement with the bed elevation changes, and the enhancement of water content at lower elevations provides a decrease in the friction coefficient in the corresponding areas.

Finally, two areas can be distinguished in the bedrock, where basal ice is frozen to the bed (0 km < x <20 km) and where there is basal sliding (25 km < x < 40 km) due to the till layer. The boundary of transition from the area of the frozen basal ice to the area of the basal sliding is diluted due to smoothing of the inverted friction coefficient by the stabilizer. The linear friction law provides a good agreement between the observed and modeled surface velocity distributions along the flow line. Thus, it can be conveniently applied in the applications (in particular, in the prognostic experiments).

The prognostic experiments reveal that both ice mass and ice stream extents decline for the reference time-independent mass balance (Bassford et al., 2006). These experiments demonstrate that the grounding lines have retreated at about 10 km for the three ice streams considering a time period of 500 years and a steady-state environmental impact, which is meant a constant elevation-dependent surface mass balance. The ice flow velocities in the ice streams decrease with time due to (a) diminishing of ice thicknesses (and thus decreasing driving stress) and (b) retreating of the grounding lines from the sliding zones toward the zones where ice is frozen to the bed (inverted friction coefficient distributions are considered as time-independent). Thus, the maxima of the ice flow velocities in the ice streams decrease from ~80–120 m/a to ~20–30 m/a. These trends in the ice flow velocities diminish the outgoing ice fluxes (Fig. 12) and as a result diminish the overall ice flux (Fig. 13).

The observations in the Russian High Arctic (Moholdt et al., 2012) have revealed that over the period between October 2003 and October 2009 the archipelagos have lost ice at a rate $-9.1 \pm 2.0\ Gt\ a^{-1}$. Other this period the ice loss from Severnaya Zemlya is evaluated as $-1.4 \pm 0.9\ Gt\ a^{-1}$ (Moholdt et al., 2012). The modeling shows that other this period the Academy of Sciences Ice Cap (the largest of the ten glaciers located on Severnaya Zemlya) could lose about $0.2..0.3\ Gt\ a^{-1}$ (Fig. 13).

5. Conclusions

The modeled present ice temperatures (Figure 5) are qualitatively the same in the three cross-sections. There are resembling zones of relatively cold ice that can be distinguished in the modeled temperatures in the middle of the cross-sections. These cold ice zones reflected the surface temperature minimum about 150–200 years ago in the inverted past temperature history (Nagornov et al., 2005, 2006). This surface temperature minimum corresponds to an event that is known as Little Ice Age.

The inversions of the friction coefficient performed for the three cross-sections can be interpreted as follows. The two levels that are evidently distinguished in the inverted friction coefficient distributions (Figure 6) can be explained by changing the physical properties of the bedrock along the flow lines. Similarly, the large values of the friction coefficient at 0 km < x < 20 km justify the rock-type bottom where ice is frozen to the bed (the ice temperature at 0 km < x <20 km is lower than the melting point). The lower values of the friction coefficient at 25 km < x <40 km presumably indicate the existence of the till layer (or the sandy layer) at the bottom. Specifically, the till layer provides the basal ice sliding.

The prognostic experiments carried out with the reference mass balance (Bassford et al., 2006) show that the grounding line has been retreated at about 10 km in the three ice streams considering a time period of 500 years. Similarly, the grounding line retreats (a) along the C–C′ flow line from ~43 km to ~37 km (the distance from the summit), (b) along the B–B′ flow line from ~40 km to ~30 km, and (c) along the D–D′ flow line from ~41 km to ~32 km considering a time period of 500 years and assuming time-independent mass balance. In the experiments, the ice flow velocities in the ice streams decrease with time due to (a) diminishing of the ice thicknesses and (b) retreating of the grounding lines from the sliding zones toward the zones where ice is frozen to the bed. Thus, the maxima of the ice flow velocities in the ice streams decrease from ~80–120 m/a to ~20–30 m/a. These trends in the ice flow velocities diminish the outgoing ice fluxes and as a result diminish the overall ice flux (Figure 13). The modeled evolution of the ice streams is in agreement with observations of ice mass loss on Severnaya Zemlya archipelago (Moholdt et al., 2012).

Acknowledgements. The authors are grateful to Prof. J.A. Dowdeswell et al. for the data that have been used in the manuscript. The authors are grateful to Prof. F. Puttyn for the useful comments to the manuscript. The authors are grateful to Dr. T. Dunse and to the anonymous referee for the reviewing the manuscript.

References

Arkhipov S.M.: Data Bank "Deep drilling of glaciers: Soviet-Russian Projects in Arctic, 1975–1990", Data of Glaciological Studies, 87, 229–238, 1999.

Arthern R. and H. Gudmundsson: Initialization of ice-sheet forecasts viewed as an inverse Robin problem, J. Glaciol, 56, 527-533, 2010.

Bassford R.P., M.J. Siegert, J.A. Dowdeswell, J. Oerlemans, A.F. Glazovsky and Y.Y. Macheret: Quantifying the Mass Balance of Ice Caps on Severnaya Zemlya, Russian High Arctic I: Climate and Mass Balance of the Vavilov Ice Cap, Arctic, Antarctic, and Alpine Research, 38 (1), 1-12, 2006.

Bassis J.N., H.A. Fricker, R. Coleman, J.-B. Minster: An investigation into the forces that drive ice-shelf rift propagation on the Amery Ice Shelf, East Antarctica, J. Glaciol, 54, 17-27, 2008.

Cuffey K. and W.S.B. Paterson: The physics of glaciers, 4th ed., Butterworth-Heineman, Elsevier, 2010.

Bindschadler R.: The importance of pressurized subglacial water in separation and sliding at the glacier bed, J. Glaciol, 29(101), 3-19, 1983.

Boulton G.S.: Processes of glacier erosion on different substrata, J. Glaciol, 23(89), 15-38, 1979.

Boulton G.S. and A.S. Jones: Stability of temperate ice caps and ice sheets resting on beds of deformable sediment, J. Glaciol, 24(90), 29-43, 1979.

Budd W.E., P.L. Keage and N.A. Blundy: Empirical studies of ice sliding, J. Glaciol, 23(89), 157-170, 1979.

Colinge J., H. Blatter: Stress and velocity fields in glaciers: Part I. Finite difference schemes for higher-order glacier models, J. Glaciol, 44, 448–456, 1998.

Dowdeswell J.A., R.P. Bassford, M.R. Gorman, M. Williams, A.F. Glazovsky, Y.Y. Macheret, A.P. Shepherd, Y.V. Vasilenko, L.M. Savatyugin, H.W. Hubberten and H. Miller: Form and flow of the Academy of Sciences Ice Cap, Severnaya Zemlya, Russian High Arctic. J. Geophys Res, 107, 1-15, 2002.

Engelhardt H.F., W.D. Harrison, and B. Kamb: Basal sliding and conditions at the glacier bed as revealed by bore-hole photography, J. Glaciol, 20(84), 469-508, 1978.

Engelhardt, H.F., B. Kamb, C.F. Raymond, and W.D. Harrison: Observation of basal sliding of Variegated Glacier, Alaska, J. Glaciol, 23(89), 406-407, 1979.

Engelhardt H. and B. Kamb: Basal sliding of Ice Stream B, West Antarctica, J. Glaciol, 44(147), 223-230, 1998.

Gagliardini O., M. Jay-Allemand, F. Gillet-Chaulet: Friction distribution at the base of a surging glacier inferred from an inverse method, San Francisco, CA, USA, AGU Fall Meeting, 2010 Dec. 13-17, Abstract: C13A-0540.

Gudmundsson G.H.: Ice-stream response to ocean tides and the form of the basal sliding law, The Cryosphere, 5, 259–270, 2011.

Habermann M., D.A. Maxwell, M. Truffer: A principled stopping criterion for the reconstruction of basal properties in ice sheets. San Francisco, CA, USA, AGU Fall Meeting, 2010 Dec. 13-17, Abstract: C21C-0556.

Hewitt I.J.: Modelling distributed and channelized subglacial drainage. The spacing of channels, J. Glaciol., 57(202), 302–314, doi:10.3189/002214311796405951, 2011.

Hoffman M. and S. Price: Feedbacks between coupled subglacial hydrology and glacier dynamics, J. Geophys. Res.: Earth Surf., 119, doi: 10.1002/2013JF002943, 2014.

Iken A.: The effect of the subglacial water pressure on the sliding velocity of a glacier in an idealized numerical model, J. Glaciol., 27(97), 407–421, 1981.

Iverson N. R., T. S. Hooyer, R. W. Baker: Ring-shear studies of till deformation: Coulomb-plastic behavior and distributed strain in glacier beds, J. Glaciol., 44:634–642, 1998.

Jansson P.: Water pressure and basal sliding on Storglaciären, northern Sweden, J. Glaciol., 41(138), 232–240, 1995.

Jay-Allemand M., F. Gillet-Chaulet, O. Gagliardini, M. Nodet: Investigating changes in basal conditions of Variegated Glacier prior to and during its 1982-1983 surge, Cryosphere, 5, 659-672, 2011.

Knight P.G.: Glaciers, Stanley Thornes, Cheltenham, UK, 1999.

Konovalov Y.V.: Inversion for basal friction coefficients with a two-dimensional flow line model using Tikhonov regularization, Research in Geophysics, 2:e11, 82-89, 2012.

Larour E., H. Seroussi, M. Morlighem, E. Rignot: Continental scale, high order, high spatial resolution, ice sheet modeling using the Ice Sheet System Model (ISSM), J Geophys Res, 117, 1-20, 2012.

Li X., Bo Sun, M.G. Siegert, R.G. Bingham, X. Tang, D. Zhang, X. Cui, X. Zhang: Characterization of subglacial landscapes by a two-parameter roughness index, J. Glaciol, 56(199), 831–836, 2010.

Leonov A.S.: Some a posteriori termination rules for the iterative solution of linear ill-posed problems. Comput Math Math Phys, 34, 121-126, 1994.

MacAyeal D.R.: Large-scale ice flow over a viscous basal sediment: theory and application to ice stream B, Antarctica, J Geophys Res, 94, 4071–4088, 1989.

MacAyeal D.R.: The basal stress-distribution of Ice Stream-E, Antarctica, inferred by control methods, J Geophys Res, Solid Earth, 97, 595-603, 1992.

Moholdt, G., B. Wouters, A. S. Gardner: Recent mass changes of glaciers in the Russian High Arctic, Geophys. Res. Lett., 39, L10502, doi:10.1029/2012GL051466, 2012.

Morlighem M., E. Rignot, H. Seroussi, E. Larour, H. Ben Dhia and D. Aubry: Spatial patterns of basal drag inferred using control methods from a full-Stokes and simpler models for Pine Island Glacier, West Antarctica, Geophys Res Lett, 37, L14502, doi:10.1029/2010GL043853, 2010.

Nagornov O.V., Y.V. Konovalov, V. Tchijov: Reconstruction of past temperatures for Arctic glaciers subjected to intense subsurface melting, Ann Glaciol, 40, 61-66, 2005.

Nagornov O.V., Y.V. Konovalov, V. Tchijov: Temperature reconstruction for Arctic glaciers, Palaeogeogr Palaeoclimatol Palaeoecol, 236, 125-134, 2006.

Nye J. F.: Water flow in glaciers: jökulhlaups, tunnels and veins, J. Glaciol, 17(76), 181–207, 1976.

Paterson W.S.B. and G.K.S. Clarke: Comparison of theoretical and observed temperatures profiles in Devon Island ice cap, Canada, Geophys. J. of R. Astron. Soc., 55(3), 615-632, 1978.

Pattyn F.: Ice-sheet modeling at different spatial resolutions: focus on the grounding zone, Ann Glaciol, 31, 211-216, 2000.

Pattyn F.: Transient glacier response with a higher-order numerical ice-flow model, J. Glaciol, 48, 467-477, 2002.

Pattyn F., L. Perichon, A. Aschwanden, B. Breuer, B. de Smedt, O. Gagliardini, G.H. Gudmundsson, R.C.A. Hindmarsh, A. Hubbard, J.V. Johnson, T. Kleiner, Y. Konovalov, C. Martin, A.J. Payne, D. Pollard, S. Price, M. Rückamp, F. Saito, O. Souček, S. Sugiyama and T. Zwinger: Benchmark experiments for higher-order and full-Stokes ice sheet models (ISMIP–HOM), The Cryosphere, 2, 95-108, 2008.

Pattyn, F., C. Schoof, L. Perichon, R. C. A. Hindmarsh, E. Bueler, B. de Fleurian, G. Durand, O. Gagliardini, R. Gladstone, D. Goldberg, G. H. Gudmundsson, P. Huybrechts, V. Lee, F. M. Nick, A. J. Payne, D. Pollard, O. Rybak, F. Saito, and A. Vieli: Results of theMarine Ice Sheet Model Intercomparison Project, MISMIP, The Cryosphere, 6(3):573–588, 2012.

Röthlisberger H.: Water pressure in intra- and subglacial channels, J. Glaciol., 11(62), 77–203, 1972.

Sergienko O.V., R.A. Bindschadler, P.L. Vornberger, D.R. MacAyeal: Ice stream basal conditions from block-wise surface data inversion and simple regression models of ice stream flow: Application to Bindschadler Ice Stream, J Geophys Res, 113, 1-11, 2008.

Schoof, C.: Ice sheet grounding line dynamics: Steady states, stability, and hysteresis, J. Geophys. Res., 112, 1–19, doi:10.1029/2006JF000664, 2007.

Sergienko, O. V. and R. C. A. Hindmarsh: Regular patterns in frictional resistance of ice-stream beds seen by surface data inversion, Science, 342(6162):1086–1089, 2013.

Seroussi, H., M. Morlighem, E. Larour, E. Rignot, A. Khazendar: Hydrostatic grounding line parameterization in ice sheet models, The Cryosphere, 8, 2075–2087, 2014.

Tikhonov A.N., V.Ia. Arsenin: Solutions of ill posed problems, Washington: Winston & Sons, 1977.

Tulaczyk, S., W. B. Kamb, H. F. Engelhardt: Basal mechanics of Ice Stream B, West Antarctica I. Till mechanics. J. Geophys. Res., 105:463–482, doi:10.1029/1999JB900329, 2000.

Van der Veen CJ. Longitudinal stresses and basal sliding: a comparative study. In: Van der Veen C.J., Oerlemans J., (eds). Dynamics of the West Antarctic ice sheet. Dordrecht: D. Reidel Publishing Co., 223-248, 1987.

Vieli A., M. Funk, H. Blatter: Flow dynamics of tidewater glaciers: a numerical modelling approach, J. Glaciol., 47(159), 595–606, 2001.

Weertman J.: On the sliding of glaciers, J. Glaciol., 3(21), 33–38, 1957.

Zagorodnov V.S.: Recent Soviet activities on ice core drilling and core investigations in Arctic region. Bulletin of Glacier Research, Data Center for Glacier Research, Japanese Society of Snow and Ice, 6, 81–84, 1988.

Figure 1 (after Dowdeswell et al. (2002)). Map of Severnaya Zemlya showing the Academy of Sciences Ice Cap on Komsomolets Island together with the other ice caps in the archipelago: Rusanov Ice Cap, Vavilov Ice Cap, Karpinsky Ice Cap, University Ice Cap, Pioneer Glacier, Semenov-Tyan Shansky Glacier, Kropotkin Glacier, Leningrad Glacier. Inset is the location of Severnaya Zemlya and the nearby Russian Arctic archipelagos of Franz Josef Land and Novaya Zemlya within the Eurasian High Arctic.

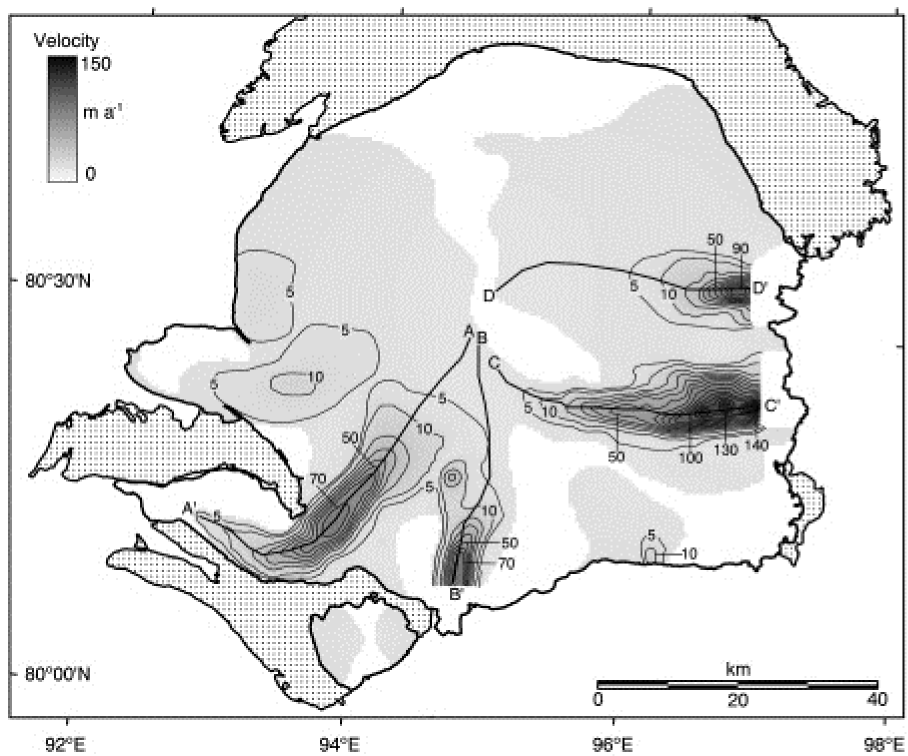

Figure 2 (after Dowdeswell et al. (2002)). Corrected interferometrically derived ice surface velocities for the Academy of Sciences Ice Cap. The first two contours are at velocities of 5 and 10 m a^{-1}, with subsequent contours at 10 m a^{-1} intervals. The unshaded areas of the ice cap are regions of non-corrected velocity data. The dotted areas represent bare land. The four fast flowing ice stream central lines are denoted as A-A', B-B', C-C', D-D', respectively. Velocity profiles A-A' to D-D' are shown in Figure 11 of Dowdeswell et al. (2002)

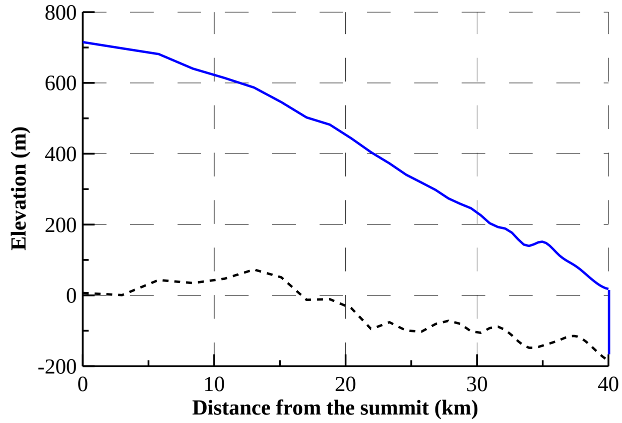

Fig. 3 (a)

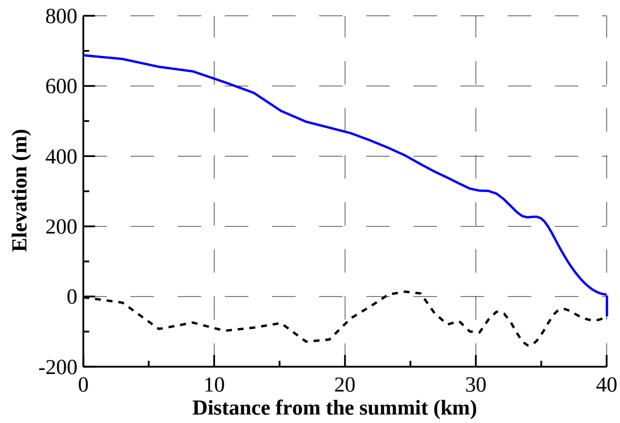

Fig. 3 (b)

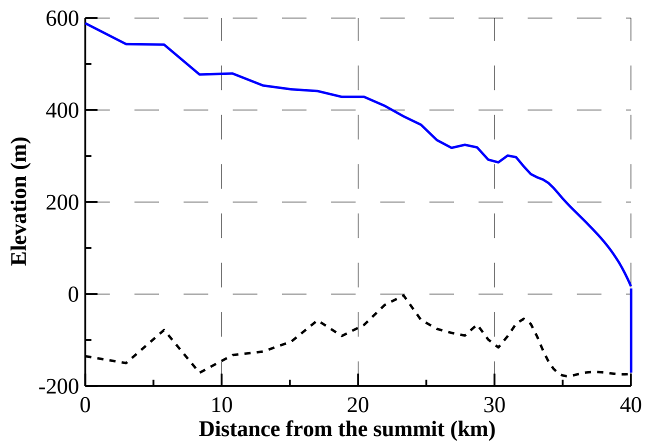

Fig. 3 (c)

Figure 3. (a) B-B' flow line profile, which crosses downstream one of the four fast flowing ice streams in the Academy of Sciences Ice Cap (Fig. 2). **(b)** C-C' flow line profile. **(c)** D-D' flow line profile. The data of ice surface and ice bed elevations are imported from Figure 8 of Dowdeswell et al. (2002).

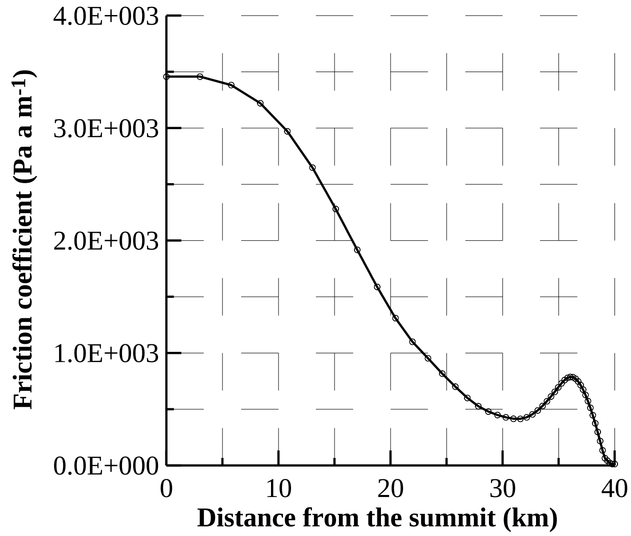

Fig. 4 (a)

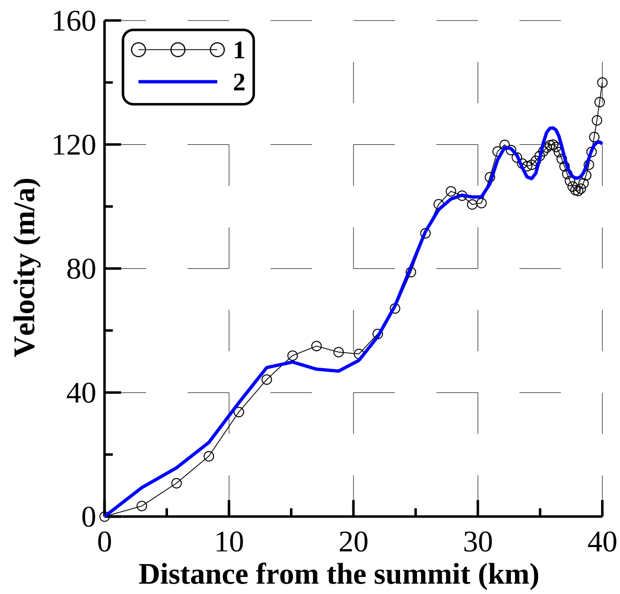

Fig. 4 (b)

Figure 4. (a) The friction coefficient distribution are obtained in the inverse problem for *the linear friction law* and for the observed surface velocity distribution along the C-C' flow line. **(b)** The ice surface horizontal velocity distributions along the flow line: **1** – the observed surface velocity distribution, taken from Figure 11 of Dowdeswell et al**.** (2002), **2** - the modeled surface velocity distribution, which corresponds to the reconstructed friction coefficient in Fig. 4,a.

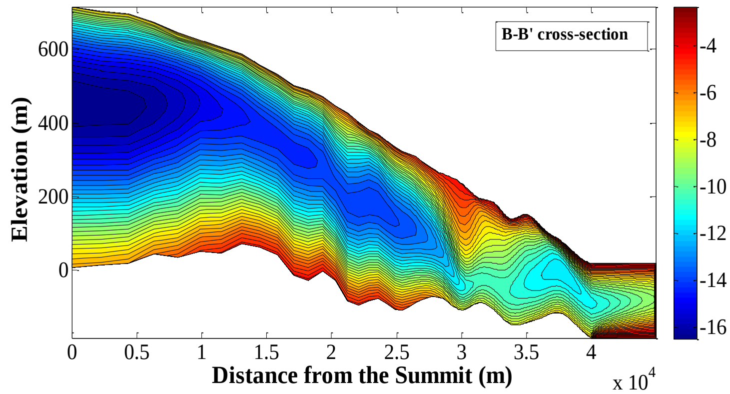

Fig. 5 (a)

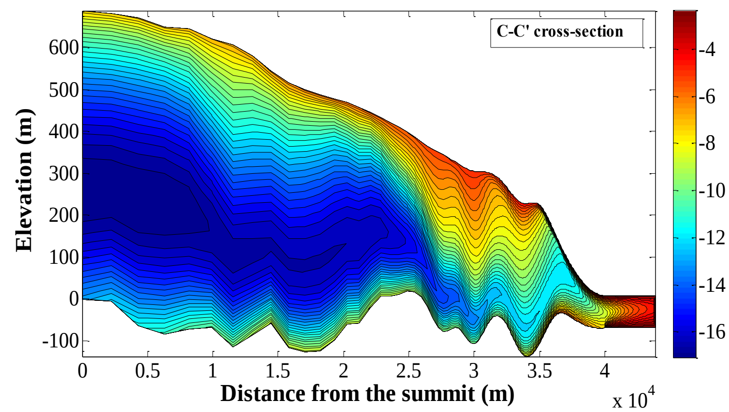

Fig. 5 (b)

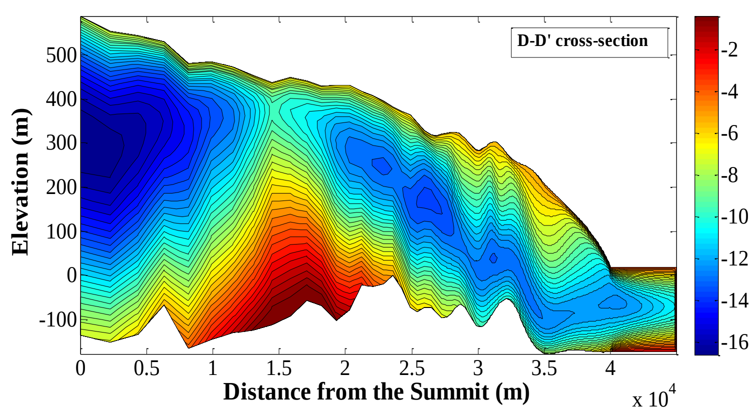

Fig. 5 (c)

Figure 5. The temperature distributions within (**a**) the B-B' cross-section, (**b**) C-C' cross-section and (**c**) D-D' cross-section simulated by the model with the past surface temperature history based on the paleo-temperature, which is retrieved from the borehole temperature data (Nagornov et al., 2005, 2006).

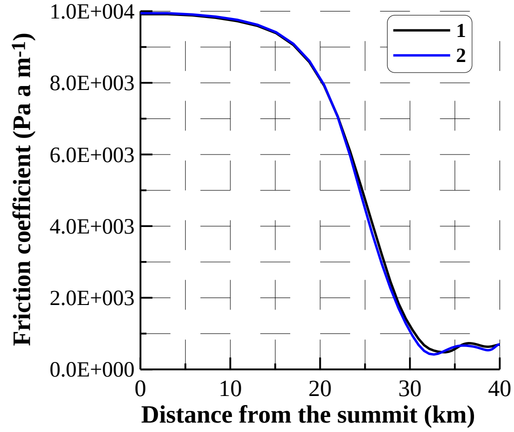

Fig. 6 (a)

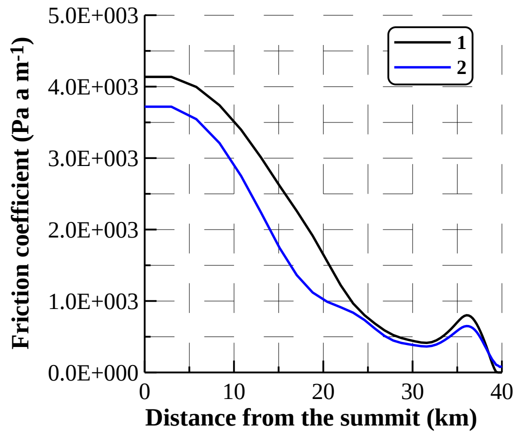

Fig. 6 (b)

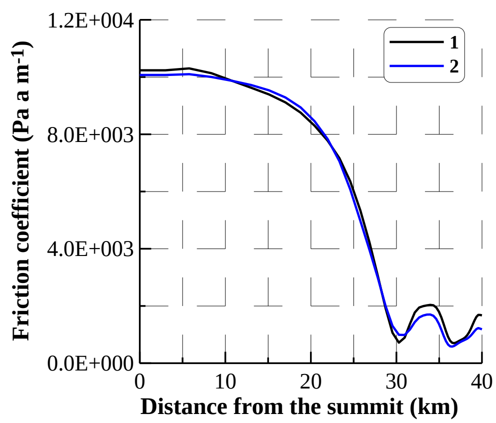

Fig. 6 (c)

Figure 6. The friction coefficients inverted along (**a**) B-B' flow line, (**b**) C-C' flow line and (**c**) D-D' flow line. Curve **1** is the first inversion, which is obtained for the linear ice temperature profiles (the ice temperature approximation for the initial inversions). Curve **2** is the second inversion, which corresponds to the modeled ice temperature (Fig. 5).

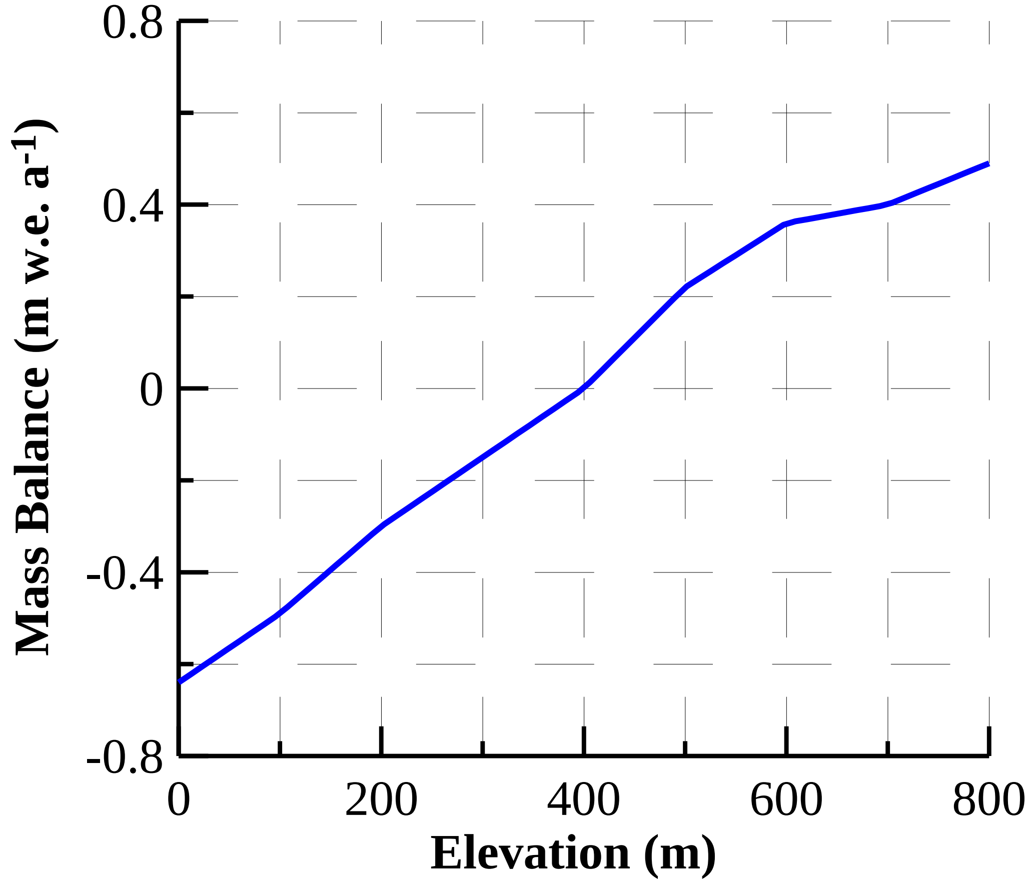

Figure 7. The surface mass balance elevational distribution along the C-C' flow line (Bassford et al., 2006).

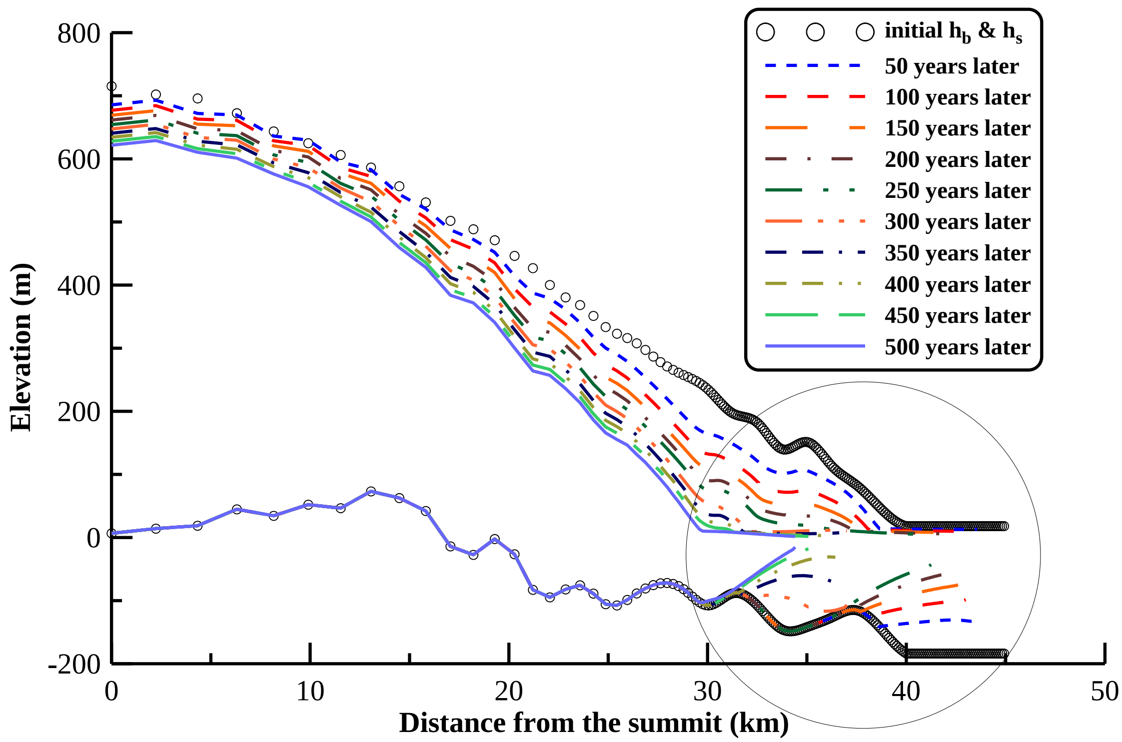

Fig. 8 (a)

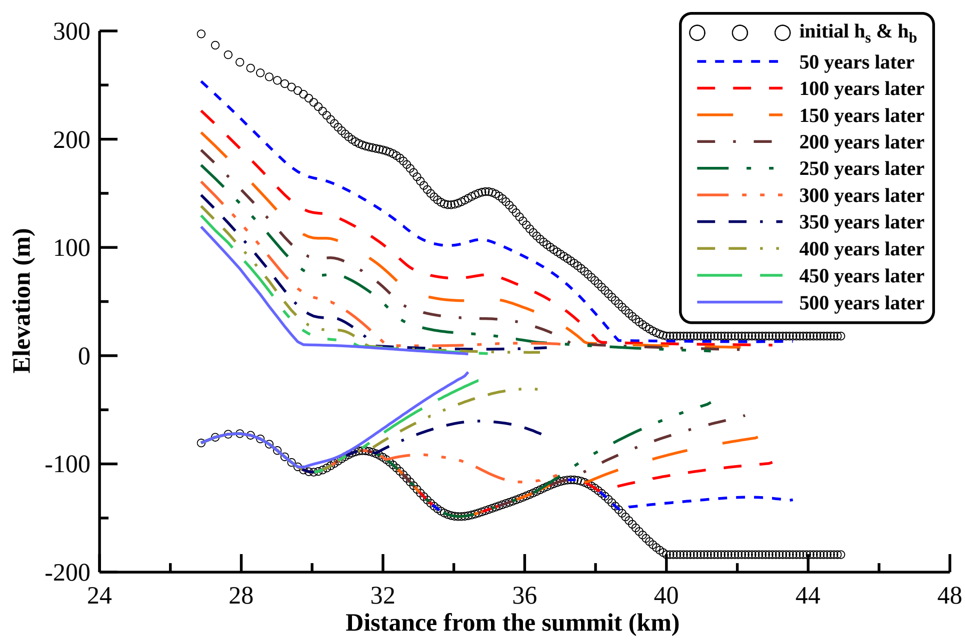

Fig. 8 (b)

Figure 8. (a) The modeled successive B-B' cross-section geometries separated by 50-year intervals from the present to the future 500 years later. (**b**) A magnified section of panel (a), showing the evolution of B-B' ice shelf.

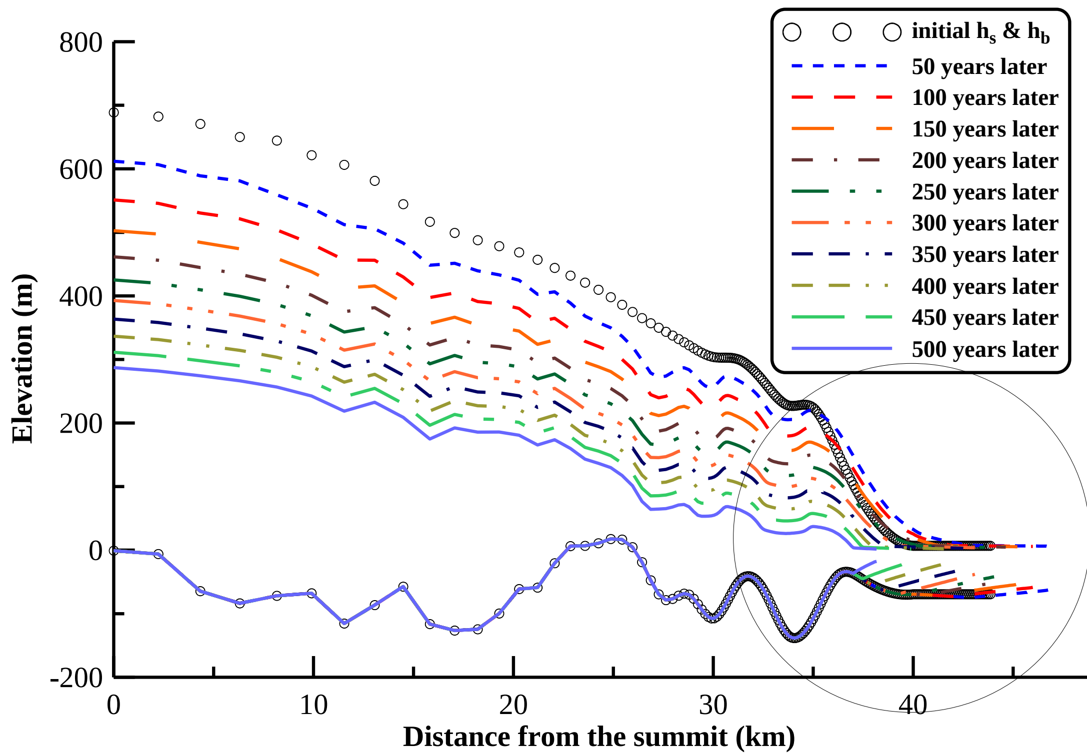

Fig. 9 (a)

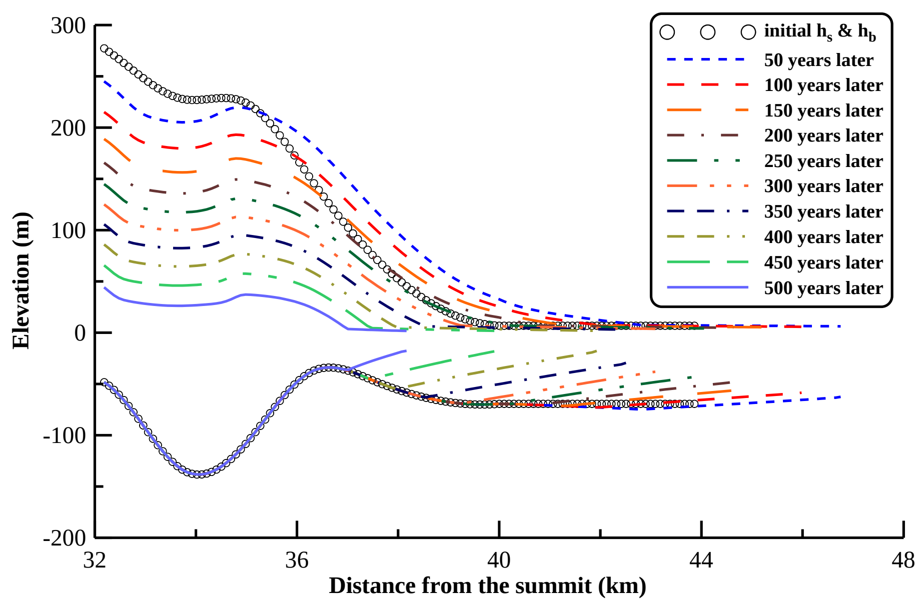

Fig. 9 (b)

Figure 9. (a) The modeled successive C-C' cross-section geometries separated by 50-year intervals from the present to the future 500 years later. (**b**) A magnified section of panel (a), showing the evolution of C-C' ice shelf.

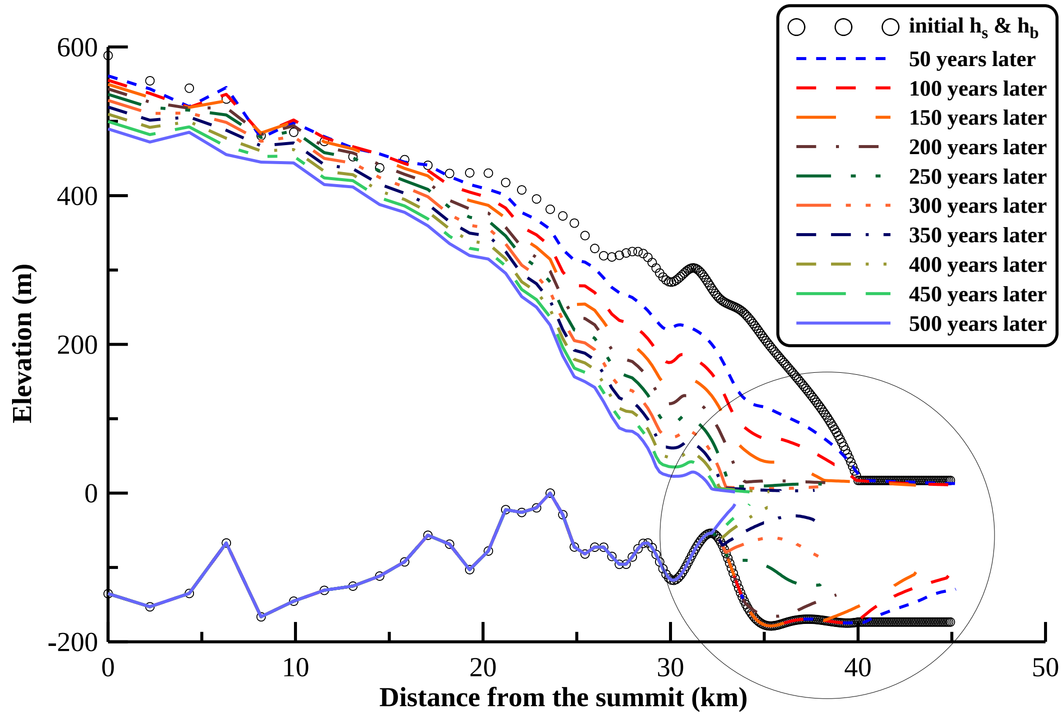

Fig. 10 (a)

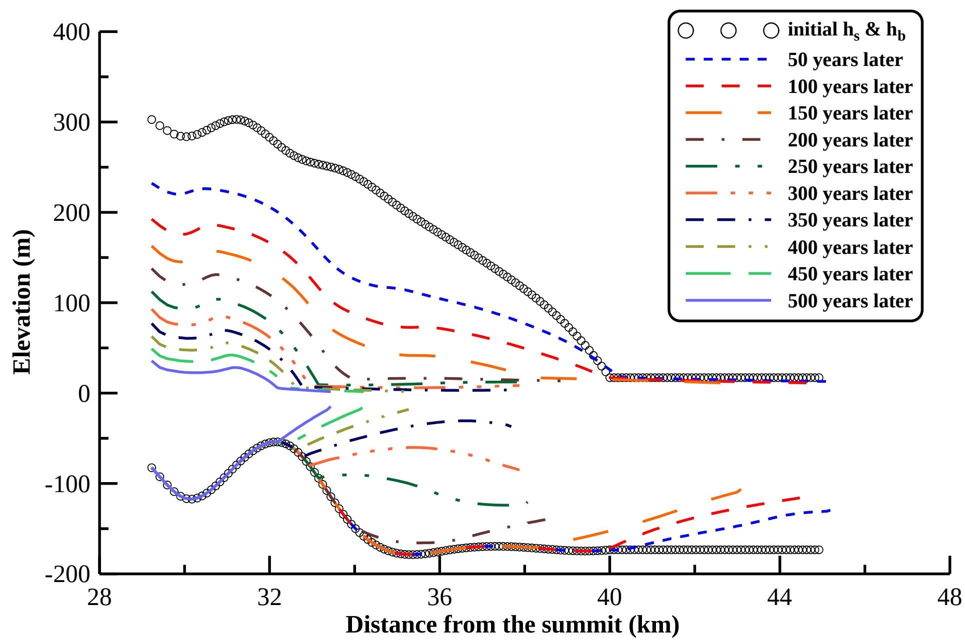

Fig. 10 (b)

Figure 10. (a) The modeled successive D-D' cross-section geometries separated by 50-year intervals from the present to the future 500 years later. (**b**) A magnified section of panel (a), showing the evolution of D-D' ice shelf.

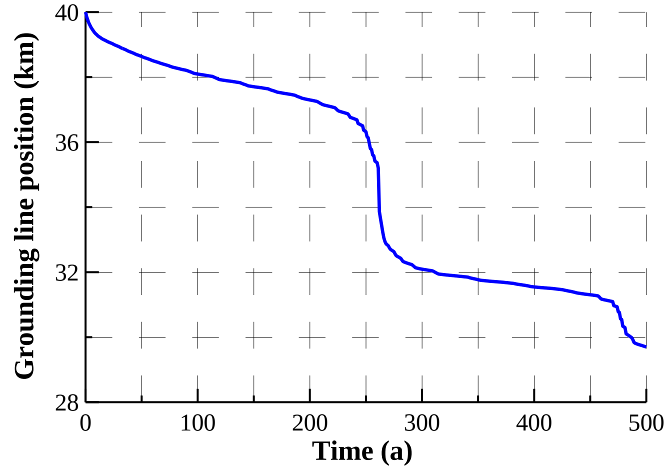

Fig. 11 (a)

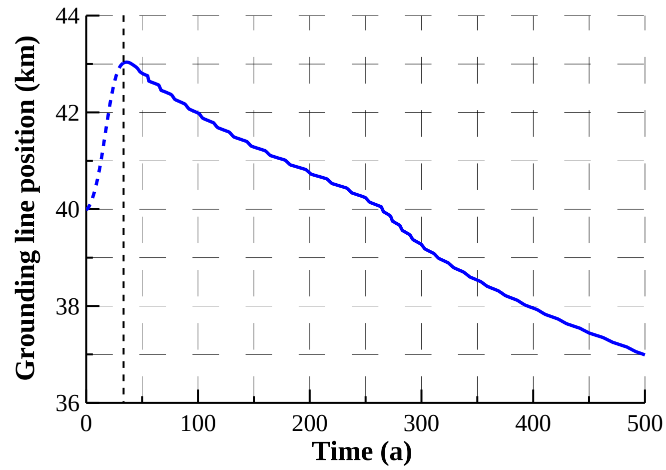

Fig. 11 (b)

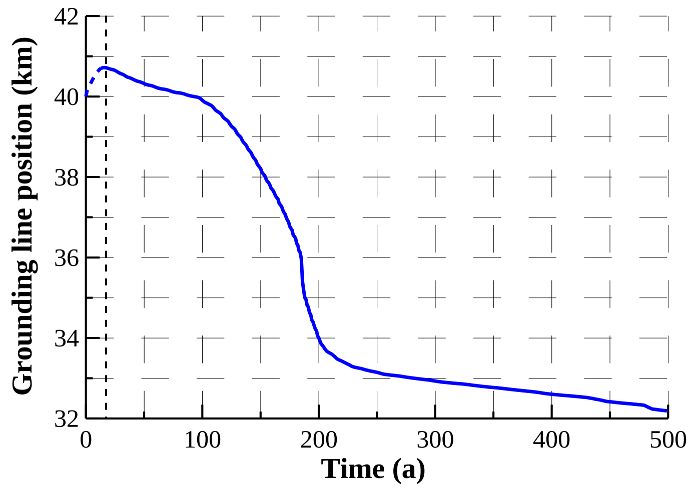

Fig. 11 (c)

Figure 11. The modeled grounding line history (**a**) for B-B' cross section (**b**) for C-C' and (**c**) for D-D' cross section.

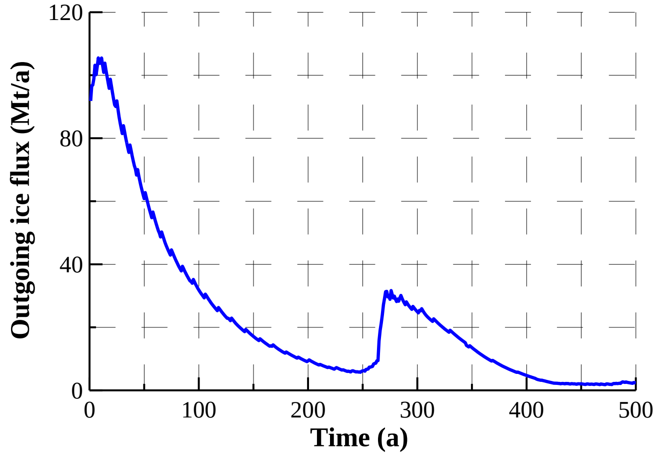

Fig. 12 (a)

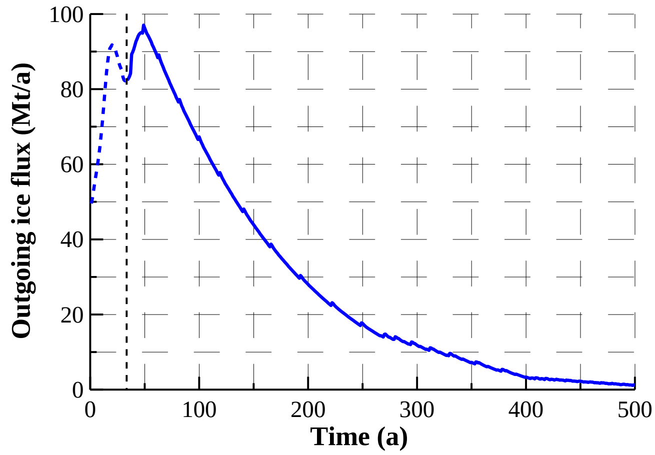

Fig. 12 (b)

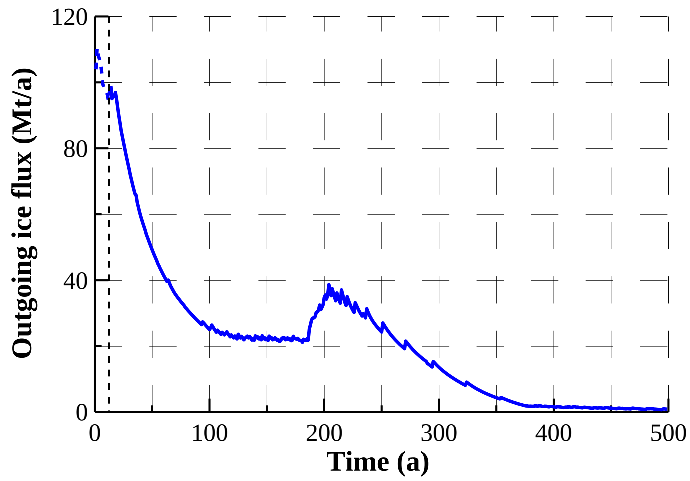

Fig. 12 (c)

Figure 12. The modeled outgoing ice flux history (**a**) for B-B' cross section (**b**) for C-C' and (**c**) for D-D' cross section.

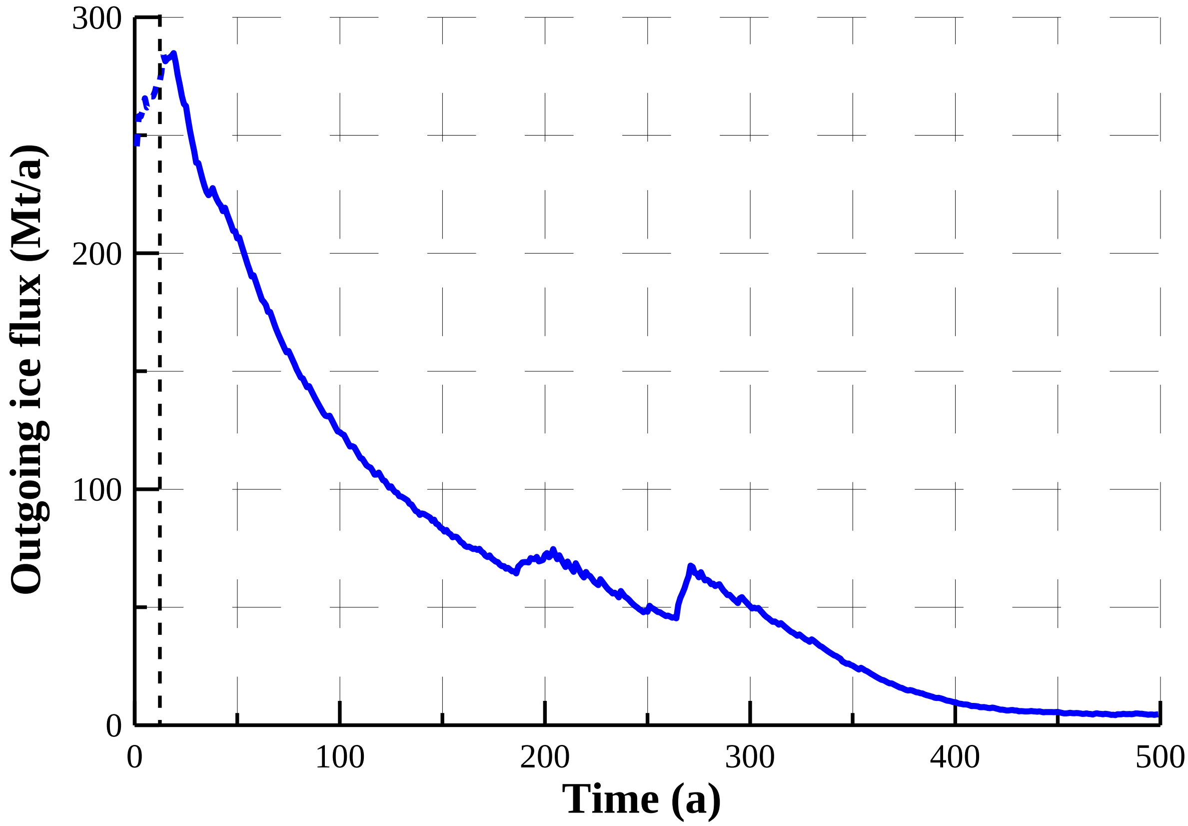

Figure 13. The overall outgoing ice flux history (the sum of the outgoing fluxes for the three ice streams: B-B', C-C' and D-D').